

Supplementary Information

Electron energy loss and angular asymmetry induced by elastic scattering in helium nanodroplets

Jakob D. Asmussen,¹ Keshav Sishodia,² Björn Bastian,¹ Abdul R. Abid,¹ Ltaief Ben Ltaief,¹ Henrik B. Pedersen,¹ Subhendu De,² Christian Medina,³ Nitish Pal,⁴ Robert Richter,⁴ Thomas Fennel,⁵ Sivarama Krishnan,² and Marcel Mudrich^{1,*}

¹*Department of Physics and Astronomy, Aarhus University, Denmark*

²*Quantum Center for Diamond and Emergent Materials (QuCenDiEM) and Department of Physics, Indian Institute of Technology Madras, Chennai 600036, India*

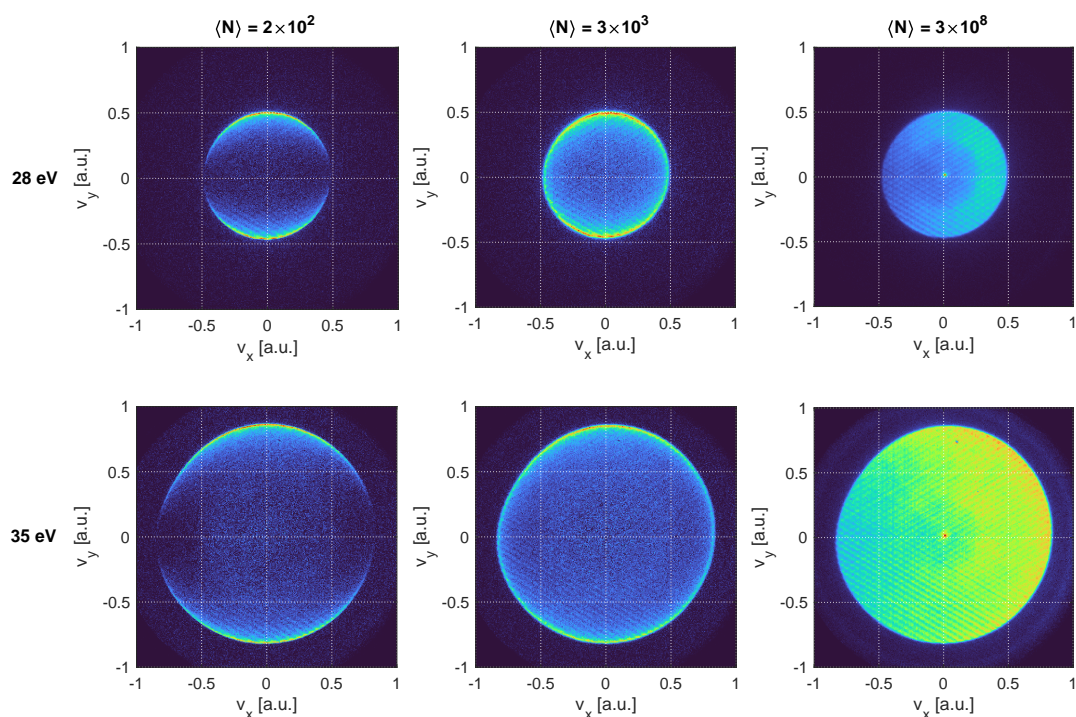
³*Institute of Physics, University of Freiburg, Germany*

⁴*Elettra Sincrotrone, Trieste, Italy*

⁵*Institut für Physik, Universität Rostock, Germany*

I. VMIS AT DIFFERENT PHOTON ENERGIES AND HND SIZES

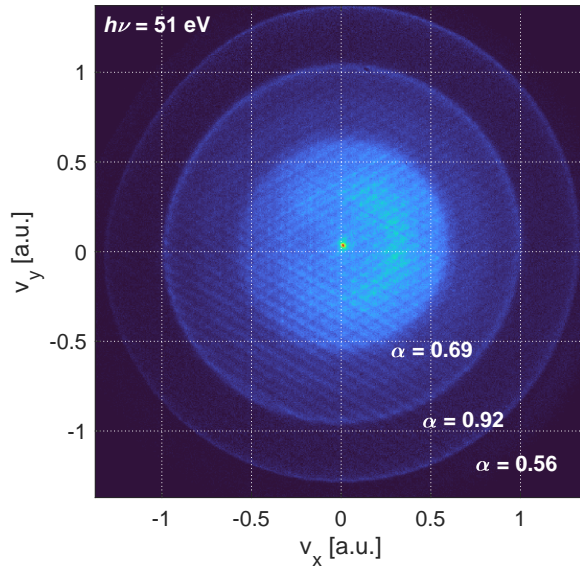
Suppl. Fig. 1 shows VMIs recorded for three different He nanodroplet sizes and two photon energies ($h\nu = 28$ eV in top row, $h\nu = 35$ eV in bottom row). They illustrate three regimes of electron emission: Slightly perturbed PAD by elastic scattering (left column), almost fully isotropic PAD (middle column), and PAD dominated by shadowing (right column).



Supplementary Fig. 1: Experimental VMIs recorded for increasing He nanodroplet sizes (left to right) and increasing photon energy (top to bottom).

Suppl. Fig. 2 shows a VMI recorded at $h\nu = 51$ eV for a droplet size of $\langle N \rangle = 2 \times 10^9$ atoms. At this photon energy, photoelectrons can inelastically scatter on He atoms in the droplets and excite or ionize another He atom in the same droplet [1]. Three ring features appear in the VMI: The outer ring reflects the photoelectrons with energy $h\nu - E_i$, where $E_i = 24.59$ eV is the ionization energy of He. The intermediate ring is due to interatomic Coulombic decay (ICD) of pairs of excited He atoms created by inelastic scattering [2]. The inner circle is due to inelastically scattered

electrons. Both photoelectrons and inelastically scattered electrons show prominent forward/backward (α) anisotropy due to the shadowing effect. The ICD electrons created by the secondary ICD reaction $\text{He}^* + \text{He}^* \rightarrow \text{He}^+ + \text{He} + e_{\text{ICD}}$ are emitted nearly isotropically ($\alpha = 0.92$). This implies that the excited He^* atoms, which are initially formed on the side of the droplet facing toward the incident light, roam around the He droplet and redistribute nearly isotropically over the droplet surface prior to the ICD reaction. Thus, this type of ICD is a slow process involving atomic motion on the length scale of the droplet circumference.



Supplementary Fig. 2: VMI recorded at $h\nu = 51$ eV for a droplet size of $\langle N \rangle = 2 \times 10^9$ atoms. The outer ring is the photoline ($h\nu - E_i$), the intermediate ring is due to electrons created by interatomic Coulombic decay of two excited He atoms and the inner circle is due to electrons inelastically scattered on another He atom in the same droplet before being emitted from the droplet. The α -parameter for each contribution is given in the figure.

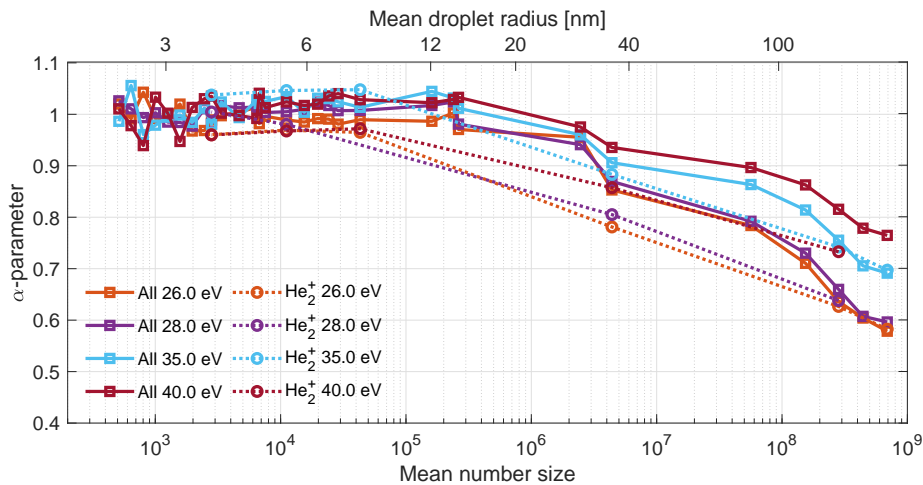
II. ANISOTROPIC EMISSION OF COINCIDENCE ELECTRONS

Suppl. Fig. 3 shows the degree of shadowing characterized by the α -parameter for all electrons and for electrons detected in coincidence with He_2^+ . In contrast to small droplets where we analyzed the β anisotropy [Figs. 2 a) and b)], the difference in α anisotropy between all electrons and electrons coincident with droplet-correlated cations is small since the atomic contribution in the beam is negligible when large droplets are formed in an expansion at low temperature ($T \leq 10$ K, expansion pressure is 30 bar).

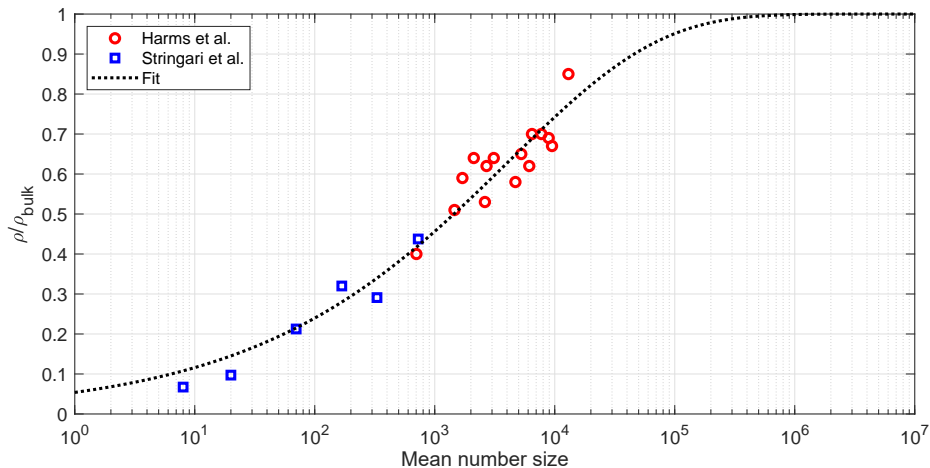
III. ELECTRON SCATTERING SIMULATION

The experimental results in this study are compared to an electron–He scattering Monte Carlo simulation based on doubly differential (energy, scattering angle) electron–He scattering cross sections [3] and the propagation of electrons along classical trajectories. In the simulation, the He number density inside the spherical droplet is assumed to be homogeneous. In reality, the droplet surface region has a variable density which crucially impacts the average density of small He clusters. We calculate the size-dependent average density in the droplet from the works of Harms *et al.* [4] and Stringari *et al.* [5]. The average density (ρ) relative to bulk density of liquid He (ρ_0) as function of droplet number size (N) is found to follow the empirical formula

$$\frac{\rho}{\rho_0} = 1 - \exp \left[- \left(\frac{N}{4155} \right)^{0.35} \right], \quad (1)$$



Supplementary Fig. 3: Anisotropy parameter α as a function of droplet size for all emitted electrons [reproduced from Fig. 2 c)] and for photoelectrons detected in coincidence with He_2^+ .

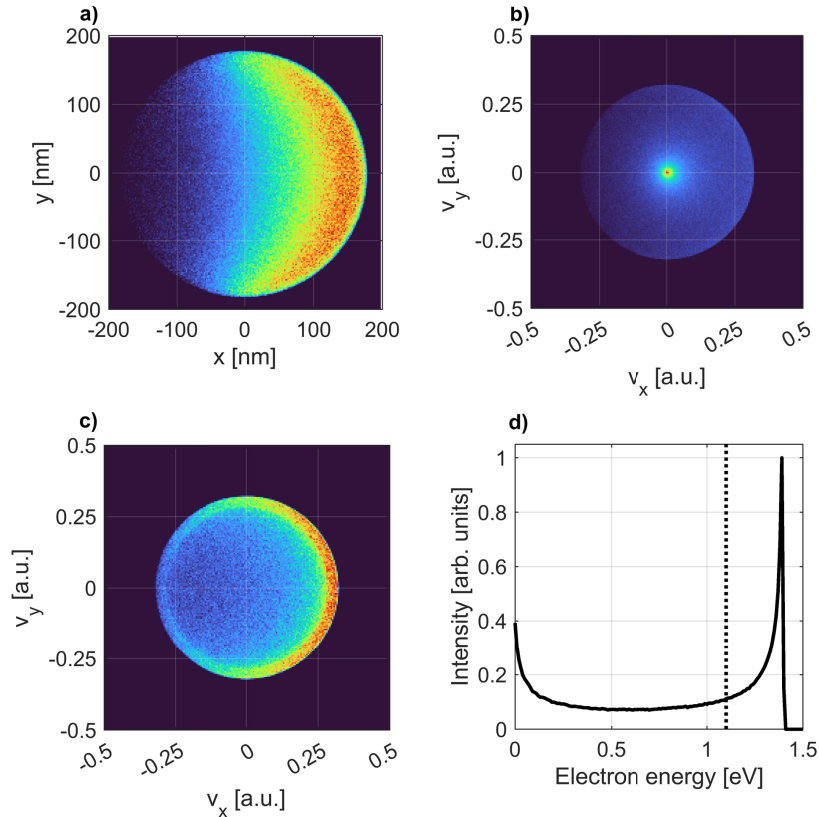


Supplementary Fig. 4: Mean He density relative to bulk density determined from fits of data reported by Harms *et al.* [4] and Stringari *et al.* [5].

see the fit curve in Suppl. Fig. 4.

In the comparison between simulation and experiment, we neglect the fact that in the experiment, droplet sizes are distributed according to a broad log-normal distribution, *i. e.* we assume $N = \langle N \rangle$ [4, 6]. The initial positions of photoelectrons are randomly selected taking into account that the photoionization probability is exponentially attenuated inside the He droplet along the direction of the photon beam according to the absorption coefficient calculated from the atomic photoionization cross section [7]. Suppl. Fig. 5 a) shows the absorption of the incoming light in a cross-sectional view of the droplet of radius $R = 170$ nm. The photon energy of the incoming light is $h\nu = 26$ eV, where the ionization cross-section of He is 6.79 Mb [7] corresponding to a penetration depth of 67.6 nm. The electron trajectory is propagated either up to a cut-off energy of 0 eV at which the electron is trapped in the Coulomb potential of the ion, or a cut-off energy 1.1 eV is included to account for solvation of the electron in the droplet which is assumed to occur at when the electron energy falls below the potential-energy barrier for electron localization [8, 9]. Suppl. Figs. 5 b) and c) show the projected velocity distribution obtained from 10^6 electron trajectories in the case of including and excluding the 1.1 eV potential barrier. Excluding the barrier results in significant overestimation of the yield low-energy electrons (LEEs) in the electron spectra. The simulated VMI obtained from only electrons with energy higher than the potential barrier [Suppl. Fig. 5 c)], the shadowing effect is clearly visible. Suppl. Fig. 5 d) shows the electron energy spectra corresponding to the VMI shown in Suppl. Fig. 5 b).

The dotted line indicates the droplet potential barrier. The simulated electron spectra for large HNDs form a bimodal distribution. When the asymmetric photoline extends down to near-zero kinetic energy, LEEs accumulate at very low energy, migrating across the droplet in a diffusive motion over a large excursion distance [see Fig. 3 c)]. This behaviour is largely unrealistic; In the real system where low-energy electron-He scattering is governed by quantum-mechanical effects and nuclear motion sets in, electrons remain trapped in the droplets by localizing in bubble states.

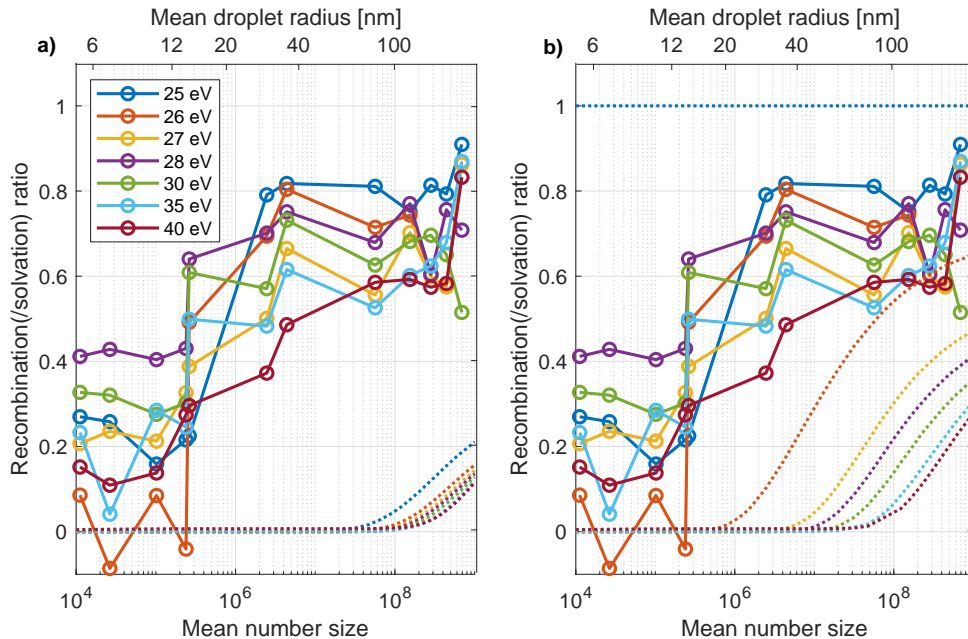


Supplementary Fig. 5: a) Cross-sectional view of the intensity distribution of the incident light onto a He droplet of radius $R = 170$ nm for at a photon energy of 26 eV. b) Projected velocity distribution of emitted electrons subjected to elastic scattering. c) Same projected distribution as in b) where electrons with kinetic energies < 1.1 eV are excluded. d) Simulated electron spectrum corresponding to the same velocity distribution. The dotted line indicates the droplet potential barrier.

IV. ESTIMATION OF THE FRACTION OF SOLVATED ELECTRONS

The proportion of electrons trapped in HNDs is hard to estimate from the experiment since we do not have a direct measure of the total photoelectrons. We estimate the total number of photoionization events by assuming that all photoelectrons are detected in the case of small droplets ($\langle N \rangle < 2 \times 10^3$) and that the total number of photoionization events is proportional to the target density in the HND beam. The relative increase in target density is determined from the stagnation pressure measured in the HND beam dump taking the beam velocity into account [10]. The shadowing effect is taken into account by integrating over the exponentially decaying photon intensity across the droplet. Suppl. Fig. 6 shows the estimated proportion of solvated (and recombined) electrons from the experimental data. The relative electron number loss starts increasing for $\langle N \rangle > 10^5$ up to $\sim 70\%$ of the electrons being trapped for $\langle N \rangle > 10^8$. Since the relative electron loss is determined indirectly relying on the forementioned assumptions, the final values have large systematic uncertainties. In Suppl. Fig. 6 a), the proportion of trapped electrons from the simulation is shown for the case that the 1.1 eV potential barrier is not taken into account and trajectories are

propagated up to electron-ion recombination occurs (dashed lines). Suppl. Fig. 6 b) shows the electron trapping in the simulation including the potential barrier. Clearly, the number of trapped electrons is grossly underestimated when the barrier is excluded. Including the potential barrier results in an electron number loss $\sim 60\%$ at $h\nu = 26$ eV for $\langle N \rangle > 10^8$. Evidently the model fails for $h\nu \leq 25.7$ eV where all electrons are trapped below the potential barrier in the simulation. In real He droplets, the He density drops to zero near the droplet surface; Clearly, a discrete 1.1 eV cut-off energy to account for electron trapping is a crude approximation. An improved model should account for the variable He density in droplets ranging from the bulk to very dilute He at the outer surface of the droplets. Additionally, quantum scattering and nuclear motion should be included.



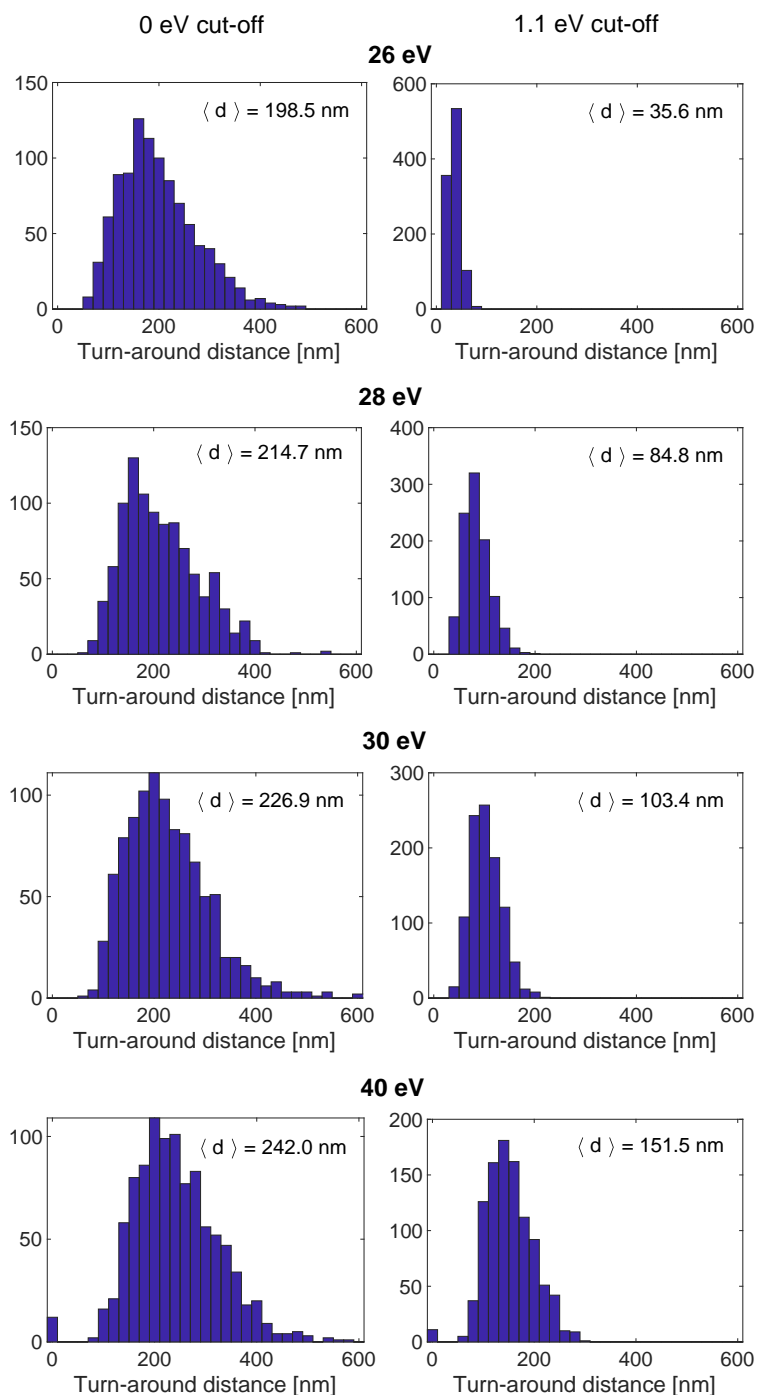
Supplementary Fig. 6: Ratio of trapped electrons to the estimated total number of photoionization events. The dotted lines show the ratio of electrons trapped in the droplets obtained from the simulation in the case of a) only including electron-ion recombination and b) introducing an energy cut-off of 1.1 eV to account for trapping of low-energy electron in the droplets.

V. ELECTRON TRAPPING RANGE

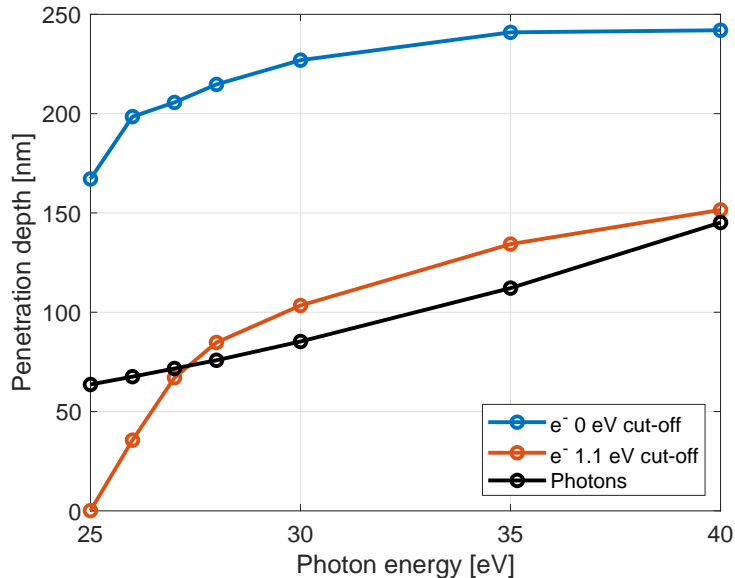
As stated in the main text, the photon penetration depth is an upper bound for the mean electron trapping range since shadowing becomes dominant when the droplet size approaches the photon penetration depth. To estimate this quantity more accurately, we determine the furthest distance that the electrons move from the cation in the simulation before turning around. Suppl. Fig. 7 shows histograms of the maximum distance between the electron and cation in the trajectory for different photon energies. We show these histograms for two conditions of electron trapping – excluding and including the droplet barrier potential. The average maximum electron-ion distance, $\langle d \rangle$, which corresponds to the mean distance the electron travels before being trapped, increases for increasing photon energy. By introducing the cut-off energy (potential barrier) of 1.1 eV, the average turn-around distance significantly drops.

Suppl. Fig. 8 shows the maximum excursion distance of the electrons from their parent ions (trapping range) as a function of photon energy for the two different cut-off criteria. For comparison, the photon penetration depth is shown, too [7]. At $h\nu = 25$ eV, the cut-off energy of 1.1 eV cannot describe the real system since all electrons are formed with less kinetic energy than the barrier potential. However, as it can clearly be seen, photoelectrons from the droplets are indeed detected in the experiment. For $h\nu < 27$ eV, the electron penetration depth (with 1.1 eV cut-off) is smaller than the photon penetration depth, and for $h\nu \geq 27$ eV the electron trapping range and photon penetration depth are comparable in magnitude. When the droplet potential barrier is disregarded, the electron trapping range

is much larger than the photon penetration depth which is inconsistent with the observation of shadowing in the experimental PAD. Therefore, the potential barrier is required to describe the electron dynamics in large HNDs.



Supplementary Fig. 7: Maximum distance travelled by the photoelectron away from the cation ('trapping range') at different photon energies. The histograms in the left column correspond to trajectories propagated until the electron energy is ≤ 0 eV (electron-ion recombination). The right column corresponds to trajectories propagated until the electron energies drop below the cut-off energy ≤ 1.1 eV accounting for solvation of the electron in the He droplet.

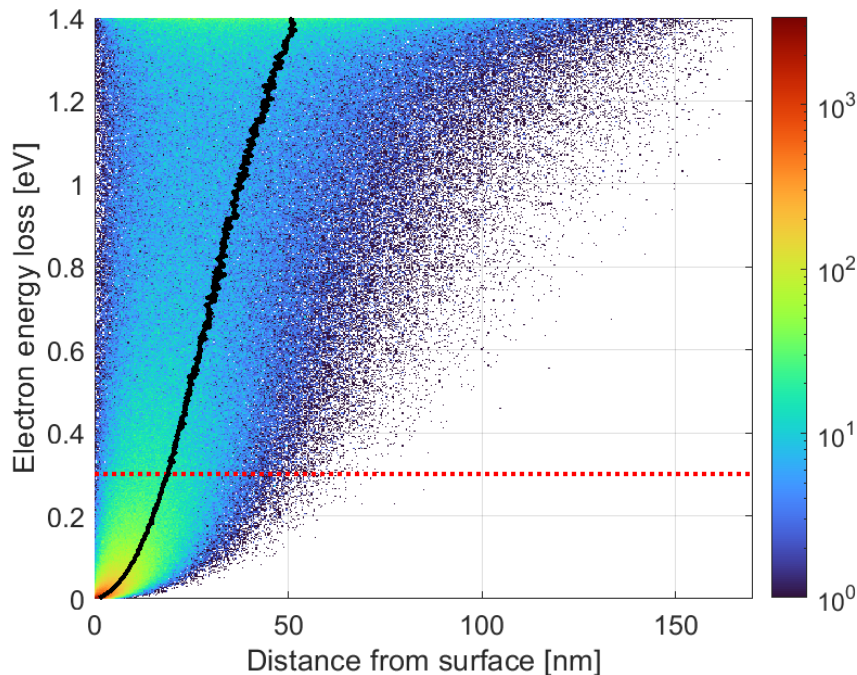


Supplementary Fig. 8: Photoelectron trapping range (blue and orange) and photon penetration depth (black) in HNDs as function of photon energy. The electron trapping range is determined from the average maximum distance that electrons travel away from their parent ions for two different electron cut-off energies.

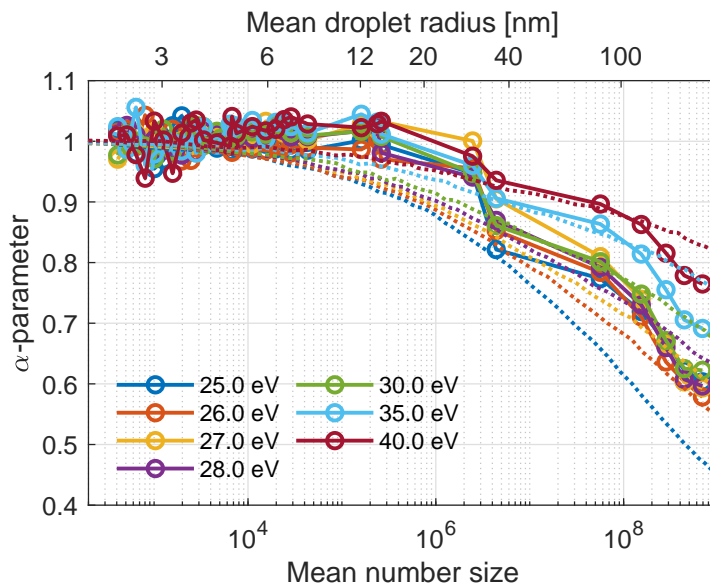
As a consequence of a limited electron mean free trapping range, only electrons formed closer to the droplet surface are more likely to escape the droplet with significant energy loss. Suppl. Fig. 9 is a density plot showing the initial distance of the photoelectron from the droplet surface as a function of simulated energy loss elastic scattering for $h\nu = 26$ eV and a droplet radius $R = 170$ nm. The average electron energy loss becomes increasingly larger the deeper into the bulk the electron is created. Implementing the potential barrier of HNDs (red dotted line) means that only electrons formed ~ 50 nm from the surface may escape the droplet. Due to the shadowing effect more electrons are formed near the surface of the droplet. Suppl. Fig. 9 also shows that electrons formed near the droplet surface either come out mostly with low energy loss or after losing most of their kinetic energy. This is because the initial electron velocity can point towards the surface or into the HND bulk where massive scattering occurs, respectively. The resulting energy distribution has a bimodal structure, see Suppl. Fig. 5 d).

The black line in Suppl. Fig. 9 shows the mean distance from the surface where an electron is formed to lose a certain amount of its kinetic energy. Thus, on average, electrons are formed $\lesssim 19$ nm from the droplet surface to be able to escape the droplet when assuming a 1.1 eV cut-off energy. This matches well the turn-around distance shown in Suppl. Fig. 7 for 26 eV. Thus, an electron with an initial kinetic energy of 1.4 eV travels a mean distance of ~ 20 nm before being trapped in liquid He. The close correlation of the 1.1 eV cut-off energy to model trapping of LEEs and the finite electron escape depth suggests that the latter could be used as an alternative condition for electron trapping. However, both the energy cut-off and an escape depth are crude model assumptions; Instead, more sophisticated models of the interaction of LEEs with superfluid He should be developed.

The α -parameter determined in the simulation for the case that the droplet potential barrier is not taken into account matches nearly equally well the experiment as α calculated including the barrier (see Suppl. Fig. 10). However, given the unphysically long excursion distance of the electron from its parent ion when no barrier is assumed, the values of the α -parameter presented in the main text are inferred from simulations including the potential barrier.



Supplementary Fig. 9: Density plot of the simulated energy loss of the escaped electrons as a function of the distance to the surface of droplet where the electron is created. The simulation is done for $h\nu = 26$ eV and $R = 170$ nm. The red dotted line shows the droplet potential barrier. The black line shows the mean distance from the surface where an electron is formed to lose a given amount of kinetic energy (y -axis).



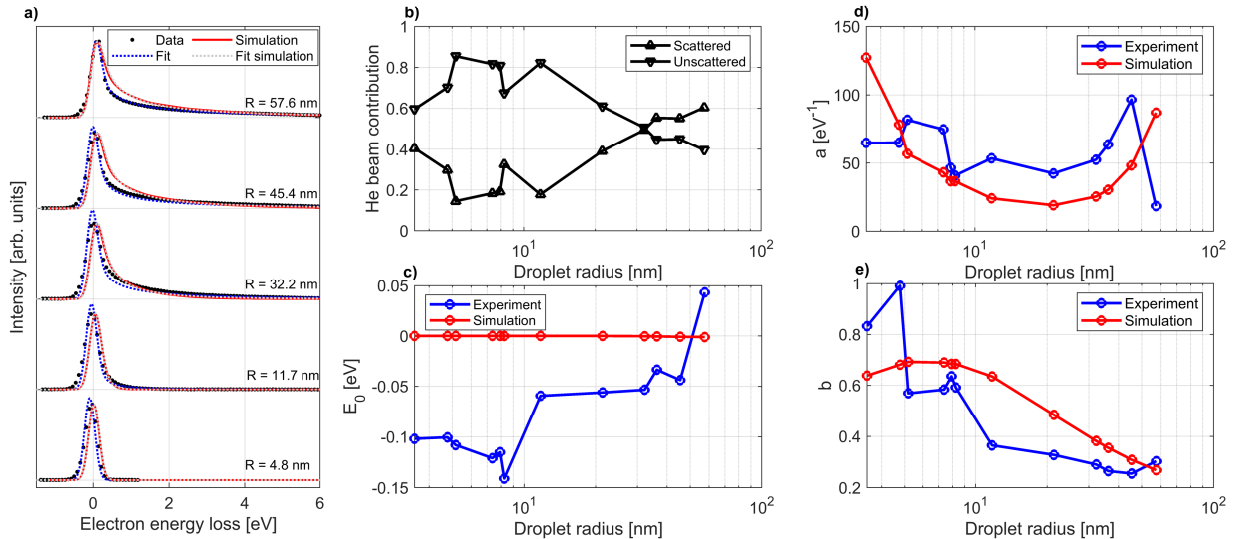
Supplementary Fig. 10: Shadowing parameter α as a function of droplet size. The dotted lines show the corresponding results of the scattering simulation for the case that the droplet potential barrier is not taken into account.

VI. FITTING OF ELECTRON SPECTRA

Electron spectra are recorded using a hemispherical analyzer at a photon energy of 44 eV. Suppl. Fig. 11 a) shows the electron energy loss for different droplet sizes. The spectra can be compared with simulated spectra which have been convoluted with a Gaussian function to account for experimental resolution. The width of the Gaussian is determined from fitting the spectra recorded for a droplet of size $R = 4.8$ nm. The electron energy loss tail is fitted using the following formula

$$f(E) = A \exp \left[- (a(E - E_0))^b \right], \quad (2)$$

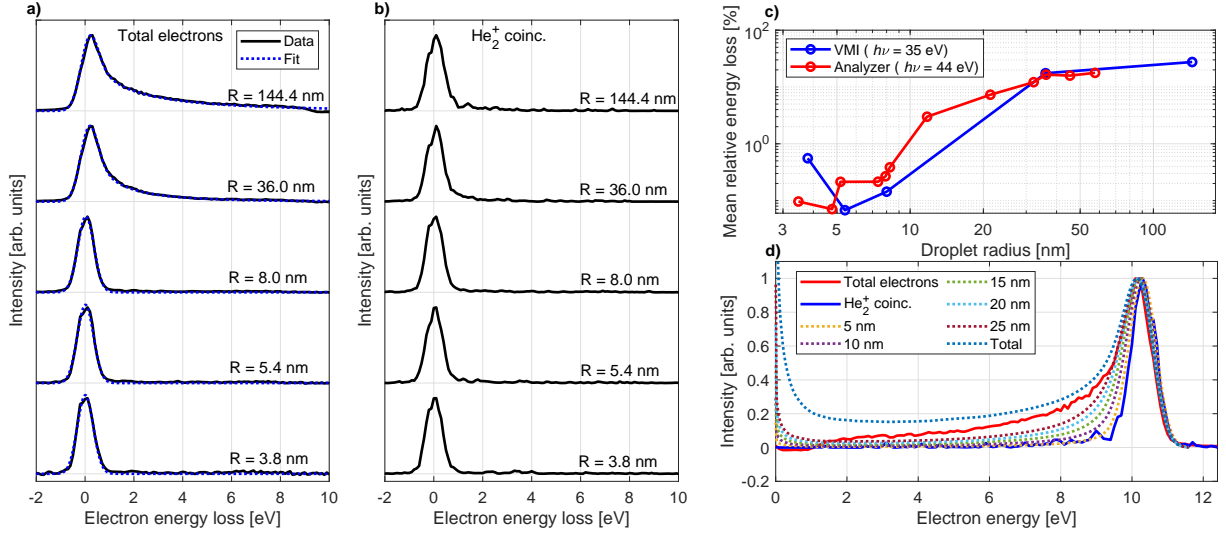
where a and b are free fit parameters with the limitation that b is required to be ≤ 1 . The fit function is numerically convoluted with a Gaussian function similarly to the simulated spectra. For the experimental curve, the fit function is augmented with an additional Gaussian function taking into account an unscattered atomic part of the droplet beam. Suppl. Fig. 11 b) shows the contribution of the scattered and unscattered part of the beam from the fit. E_0 is introduced into the function to take into account any energy shift as function of droplet size and systematic errors in the detector calibration. An energy shift on the order of 0.1 eV is found when increasing the droplet radius by one order of magnitude [Suppl. Fig. 11 c)]. The absolute position of the peak may be affected by inaccuracies in the calibration. The fit parameters defining the extension of the energy loss tail (a and b) are not found to converge to a single unique set of values. However, the average energy loss calculated from the two parameters are stable for different starting conditions of the fit. The b -parameter is larger (closer to 1) for smaller droplets matching with previous reports in the literature where the energy loss was found to be exponential for small droplets [11].



Supplementary Fig. 11: a) Measured and simulated electron spectra at $h\nu = 44$ eV for different droplet sizes and their corresponding fits. The simulated spectra are convoluted with a Gaussian function to take into account the experimental resolution which is determined from fits of the smallest-droplet spectra ($R = 4.8$ nm). b-e) Values of the fit parameters as function of droplet size. In b), only the fit parameters to the experimental data are shown because only the fit to the experimental data includes the two different contributions (scattered and unscattered).

To validate the results from the fit model, we compare spectra recorded using a hemispherical analyzer with the velocity map images (VMIs) recorded at different droplet sizes. Due to the shadowing effect, the cylindrical symmetry of the VMIs is broken for large droplets and the Abel inversion of the images is not defined [12]. To circumvent this issue, we use only the backward plane of the image for Abel inversion. Suppl. Fig. 12 a) and b) show electron loss spectra from inversion of VMIs recorded at 35 eV photon energy of all electrons and electrons in coincidence with He_2^+ -ions, respectively. The model fits the total-electron spectra well resulting in a mean relative energy loss matching the results from the spectra recorded with the hemispherical analyzer (see Suppl. Fig. 12 c). The electron spectra recorded in coincidence with He_2^+ ions show nearly no energy loss due to elastic scattering. By comparing with simulated electron spectra taking only electrons formed in a defined surface layer into account, Suppl. Fig. 12d)

shows that only electrons formed in a surface layer of thickness of 5 nm contribute to the coincidences with He_2^+ -ions. This demonstrates that He cations formed deeper inside the liquid bulk of the droplets are more likely solvated due to snowball formation [13].



Supplementary Fig. 12: a-b) Electron energy loss spectra inferred from Abel inversion of VMIs recorded at a photon energy of 35 eV for total electrons and for electrons detected in coincidence with He_2^+ . The spectra for all electrons are fitted using the outlined fit model, and the resulting mean relative energy loss is shown in c) in comparison with the size-dependent energy loss determined from the experiment using a hemispherical analyzer. d) shows the electron spectra inferred from VMIs for all electrons and for electrons detected in coincidence with He_2^+ for a droplet radius of 144.4 nm. The dotted lines show corresponding simulations taking all electrons and only electrons formed in a surface layer of thickness 5-25 nm into account.

VII. SOME ESTIMATES OF THE KINEMATICS OF ELECTRON-HELIUM SCATTERING

The maximum energy transfer in a binary elastic collision of an electron with He atoms occurs in a head-on collision. Then, the energy loss per collision is [8]

$$\Delta E = E - E' = \frac{1}{2}mv^2 - \frac{1}{2}mv'^2 = \frac{1}{2}mv^2 \left[\left(\frac{M-m}{M+m} \right)^2 - 1 \right] \approx 4E \frac{m}{M}. \quad (3)$$

Here, v and v' is the electron velocity before and after the collision, respectively, and $m = m_e$, $M = m_{\text{He}} \approx 8000 \times m_e$. Thus, for $E = 10$ eV, this yields an energy loss per collision of up to $\Delta E = 5$ meV.

The corresponding factor by which the electron energy is reduced is

$$x = \frac{E'}{E} = \frac{v'^2}{v^2} = \left(\frac{M-m}{M+m} \right)^2 \approx 1 - 4 \frac{m}{M} = 99.95\%. \quad (4)$$

Thus, it takes ≈ 300 binary head-on collisions for a 15% reduction of the electron kinetic energy.

* mudrich@phys.au.dk

- [1] M. Shcherbinin, F. V. Westergaard, M. Hanif, S. Krishnan, A. LaForge, R. Richter, T. Pfeifer, and M. Mudrich, Inelastic scattering of photoelectrons from he nanodroplets, *The Journal of chemical physics* **150**, 044304 (2019).
- [2] L. B. Ltaief, K. Sishodia, S. Mandal, S. De, S. Krishnan, C. Medina, N. Pal, R. Richter, T. Fennel, and M. Mudrich, Efficient indirect interatomic coulombic decay induced by photoelectron impact excitation in large he nanodroplets, arXiv preprint arXiv:2303.14837 (2023).

- [3] M. Adibzadeh and C. E. Theodosiou, Elastic electron scattering from inert-gas atoms, *Atomic Data and Nuclear Data Tables* **91**, 8 (2005).
- [4] J. Harms, J. P. Toennies, and F. Dalfovo, Density of superfluid helium droplets, *Phys. Rev. B* **58**, 3341 (1998).
- [5] S. Stringari and J. Treiner, Systematics of liquid helium clusters, *The Journal of Chemical Physics* **87**, 5021 (1987).
- [6] E. Knuth and U. Henne, Average size and size distribution of large droplets produced in a free-jet expansion of a liquid, *J. Chem. Phys.* **110**, 2664 (1999).
- [7] J. Samson and W. C. Stolte, Precision measurements of the total photoionization cross-sections of He, Ne, Ar, Kr, and Xe, *Journal of Electron Spectroscopy and Related Phenomena* **123**, 265 (2002).
- [8] U. Henne and J. P. Toennies, Electron capture by large helium droplets, *J. Chem. Phys.* **108**, 9327 (1998).
- [9] J. R. Broomall, W. D. Johnson, and D. G. Onn, Density dependence of the electron surface barrier for fluid He3 and He4, *Physical Review B* **14**, 2819 (1976).
- [10] L. F. Gomez, E. Loginov, R. Sliter, and A. F. Vilesov, Sizes of large He droplets, *J. Chem. Phys.* **135**, 154201 (2011).
- [11] E. Loginov, D. Rossi, and M. Drabbels, Photoelectron spectroscopy of doped helium nanodroplets, *Phys. Rev. Lett.* **95**, 163401 (2005).
- [12] B. Dick, Inverting ion images without Abel inversion: maximum entropy reconstruction of velocity maps, *Phys. Chem. Chem. Phys.* **16**, 570 (2014).
- [13] K. Atkins, Ions in liquid helium, *Physical Review* **116**, 1339 (1959).